

Characterizing the Optical Trapping of Rare Isotopes by Monte Carlo Simulation

D. H. Potterveld,¹ S. A. Fromm,^{2,*} K. G. Bailey,¹ M. Bishof,¹ D.W. Booth,¹
M. R. Dietrich,¹ J. P. Greene,¹ R. J. Holt,^{1,3} M. R. Kalita,^{1,4,†} W. Korsch,⁴ N. D. Lemke,⁵
P. Mueller,¹ T. P. O'Connor,¹ R. H. Parker,^{1,‡} T. Rabga,^{1,2} and J. T. Singh²

¹*Physics Division, Argonne National Laboratory, Argonne, Illinois 60439, USA*

²*National Superconducting Cyclotron Laboratory and Department of Physics and Astronomy,
Michigan State University, East Lansing, Michigan 48824, USA*

³*Kellogg Radiation Laboratory, California Institute of Technology, Pasadena, California 91125, USA*

⁴*Department of Physics and Astronomy, University of Kentucky, Lexington, Kentucky 40506, USA*

⁵*Department of Physics and Engineering, Bethel University, St. Paul, MN 55112, USA*

(Dated: March 20, 2019)

Optical trapping techniques are an efficient way to probe limited quantities of rare isotopes. In order to achieve the highest possible measurement precision, it is critical to optimize the optical trapping efficiency. This work presents the development of a three-dimensional semi-classical Monte Carlo simulation of the optical trapping process and its application to optimizing the optical trapping efficiency of Radium for use in the search of the permanent electric dipole moment of ²²⁵Ra. The simulation includes an effusive-oven atomic beam source, transverse cooling and Zeeman slowing of an atomic beam, a three-dimensional magneto-optical trap, and additional processes such as collisions with residual gas molecules. We benchmark the simulation against a well-characterized ⁸⁸Sr optical trap before applying it to the ²²⁵Ra optical trap. The simulation reproduces the relative gains in optical trapping efficiency measured in both the ⁸⁸Sr and ²²⁵Ra optical traps. The measured and simulated values of the overall optical trapping efficiencies for ⁸⁸Sr are in agreement; however, they differ by a factor of 30 for ²²⁵Ra. Studies of several potential imperfections in the apparatus or systematic effects, such as atomic beam source misalignment and laser frequency noise, show only limited effects on the simulated trapping efficiency for ²²⁵Ra. We rule out any one systematic effect as the sole cause of the discrepancy between the simulated and measured ²²⁵Ra optical trapping efficiencies; but, we do expect that a combination of systematic effects contribute to this discrepancy. The accurate relative gains predicted by the simulation prove that it is useful for testing planned upgrades to the apparatus.

I. INTRODUCTION

Optical trapping is now a standard technique in a variety of rare isotope applications such as searches for new physics. Examples include ground water dating with ⁸¹Kr and ³⁹Ar [1, 2], precision measurements of the charge radii of exotic ^{6,8}He nuclei [3–5], a search for new physics by probing β -decay in unstable ⁶He, ²¹Na, ³⁷K [6–8], and a search for atomic parity violation in Fr isotopes [9]. Our primary application is using optically trapped ²²⁵Ra in the search for a permanent electric dipole moment (EDM) [10] (for a recent review of EDMs see [11]). ²²⁵Ra offers enhanced sensitivity in diamagnetic atomic EDM searches due to the octupole deformation of its nucleus [12, 13]. Using optically trapped ²²⁵Ra atoms, we have measured the ²²⁵Ra EDM to be $d(^{225}\text{Ra}) < 1.4 \times 10^{-23} e \cdot \text{cm}$ [14]. In order to efficiently utilize limited quantities of ²²⁵Ra (10^{14} atoms per measurement) and to further improve the measurement statistical precision, it is essential to optimize the optical

trapping efficiency of our experimental apparatus. Since it is impractical to empirically study the effect of a multitude of parameters in our optical trapping system, we have chosen to model the apparatus using a purpose-built three-dimensional Monte Carlo (MC) simulation.

Existing simulations included some, but not all, of the features necessary to fully model our apparatus. Early simulations (ca. 1990) typically only simulated individual subsystems of an optical trapping apparatus, as the available computational resources of the era limited the complexity that could be reasonably modeled. One such MC simulation modeled atomic beam cooling, but approximations, such as assuming isotropic spontaneous emission in the presence of circularly polarized laser beams, only allowed for upper limits on the atomic beam velocity distribution to be obtained [15]. A Langevin-equation based simulation of atoms in one- and three-dimensional optical molasses predicted temperatures of cooled Na and Cs atoms in agreement with experiments, but also produced exotic results such as non-Gaussian velocity distributions [16]. As computational power increased over the following decades, simulations of the laser cooling and trapping process increased in complexity. A two-dimensional simulation [17] used multiple cooling and trapping subsystems chained together to model experiments, but did not include any additional experimental factors, such as the atomic beam source. A recent simulation [18] of the slowing of a supersonic

* fromm@nscl.msu.edu

† Present Address: TRIUMF, 4004 Wesbrook Mall, Vancouver, British Columbia V6T 2A3, Canada

‡ Present Address: Department of Physics, University of California at Berkeley, Berkeley, California 94720, USA

atomic beam incorporated a three-dimensional treatment of atoms in a laser-field, but did not include atomic beam collimation nor optical trapping. Fully quantum treatments of light-atom interactions [19, 20] used MC wavefunction techniques, but as with earlier simulations, typically only looked at individual subsystems, such as optical molasses.

In the absence of an existing simulation that could fully model our ^{225}Ra optical trap, we developed a laser cooling and trapping MC simulation that includes both the main subsystems of an optical trapping system and additional experimental details of our apparatus such as the atomic beam source. In addition to applying it to our ^{225}Ra optical trap, we benchmarked our simulation against a well-characterized ^{88}Sr optical trap used in an optical lattice clock at JILA. The simulation replicates certain performance characteristics of both optical traps, such as the relative gain in trapping efficiency from transversely cooling the atomic beam, but does not reproduce the measured overall trapping efficiency by a factor of 30 for the ^{225}Ra -optical trap.

In this work we present the decade-long development of our MC simulation and its application to our ^{225}Ra optical trap. In Sec. II we describe the experimental setups of the ^{225}Ra and ^{88}Sr optical traps considered in the simulation. Sec. III details the features of the MC simulation. We present the simulation results in Sec. IV and further systematic studies examining the discrepancy between the measured and simulated results in Sec. V. Sec. VI outlines our planned upgrades to and future use of the simulation. Our treatment of light-atom interactions, atomic beam source angular & velocity distributions, and estimates of the relevant van der Waals C_6 coefficients are detailed in Appendices A, B, and C respectively.

II. THE OPTICAL TRAPPING SYSTEMS

A. Ra optical trap

The Ra optical trap was developed and optimized at Argonne National Laboratory for use in a next-generation search for a permanent EDM [21, 22]. The optical trap is fully detailed in Refs. [10, 23, 24] and we present here an overview of the subsystems relevant to our simulation. ^{226}Ra ($\tau_{1/2} = 1600$ yr, nuclear spin = 0) is used for testing and optimizing the trap, while ^{225}Ra ($\tau_{1/2} = 15$ d, nuclear spin = $1/2$) is used for the EDM measurements.

The lowest-lying $^1S_0 \leftrightarrow ^1P_1$ transition is typically used for laser cooling of alkaline-earth atoms, e.g. Ca and Yb, but we do not use this transition for Ra due to the high probability for an atom to decay into the metastable D and P states. Instead, we use the weaker $7s^2\ ^1S_0 \leftrightarrow 7s7p\ ^3P_1$ transition near 714 nm for laser cooling and trapping, see Fig. 1 (left). This intercombination transition is weakly allowed in divalent atoms due to singlet-triplet mixing [25]; for Ra, the 3P_1 lifetime is 422 ns [26], yielding

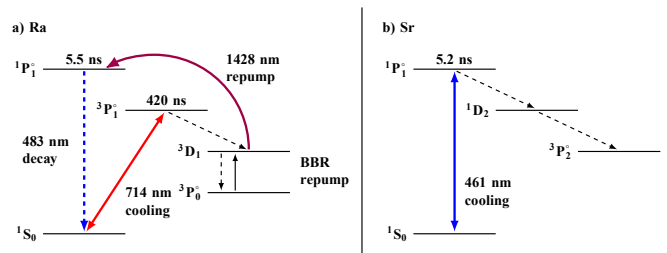


FIG. 1. Simplified level diagram for Ra (left) and Sr (right). For Ra, we handle decays to the metastable states 3D_1 and 3P_0 by a repump laser and room-temperature blackbody radiation (BBR) as described in Ref. [23]. With Sr, decay to metastable states occurs with a time constant of 20 ms, although two repump lasers (not shown) permit continued cycling on the 461 nm transition.

a natural linewidth $\gamma_{\text{Ra}}/2\pi \approx 380$ kHz. While this transition is sufficiently strong for trapping Ra atoms [23], we are only able to slow atoms with initial velocities of up to 63 m s^{-1} .

A diagram of the laser trapping portion of the apparatus is shown in Fig. 2. We heat a crucible containing metallic Ba and $\text{Ra}(\text{NO}_3)$ to about 500°C , sufficient to produce a beam of atomic Ra (chemically reduced by the Ba) that we collimate with a nozzle of length $L_{\text{noz}} = 8.3\text{ cm}$ and diameter $d_{\text{noz}} = 0.2\text{ cm}$. At this temperature, we determine the total integrated beam flux to be $5 \times 10^9\text{ s}^{-1}$ by collecting laser-induced fluorescence on a photomultiplier tube from the atomic beam approximately 27 cm downstream from the oven's nozzle. An approximate beam divergence half-angle of 13 mrad is expected based on the aspect ratio of the nozzle in the molecular flow limit.

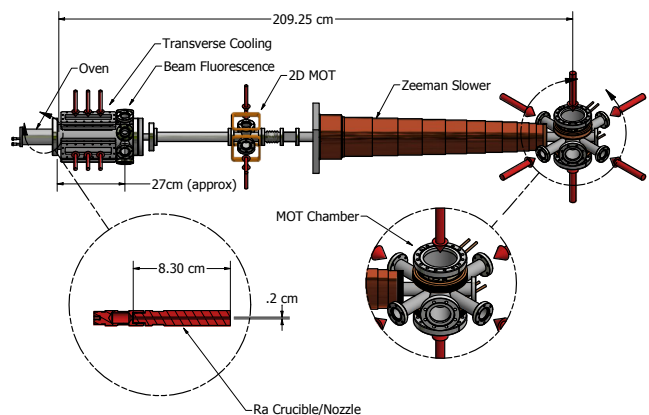


FIG. 2. Schematic diagram of the Ra optical trapping system that has been developed at the Argonne National Laboratory. The inset figures show details of the oven system and the 3D magneto-optical trap (MOT). The figure is to scale and the overall length from the output of the oven to the MOT is about 2 m.

After exiting the nozzle, the atoms are transversely cooled with a 2D optical molasses formed by two or-

thogonal laser beams each making about 10 passes across the atomic beam. The atomic beam then passes through a conductance-limiting tube with diameter 2.5 cm and length 1 cm, see Fig. 2. Subsequently, the atoms enter a 1 m long constant deceleration Zeeman slower. Here, we use a σ^+ slower configuration where the magnetic field decreases with distance as the atoms are slowed. This type of slower is appropriate for the weak transition available in Ra because it allows the slowing region to extend all the way to the magneto-optical trap (MOT). Moreover, the atoms are less affected by transverse heating during the slowing process. The Zeeman slower uses a peak field of 12 G to capture atoms with velocities up to 63 m s^{-1} . Finally, we use a three-dimensional MOT to trap the atoms, where a single repump laser beam near 1428 nm and room-temperature blackbody radiation keep the atoms cycling on the cooling transition, see Fig. 1 (left) and Ref. [23].

B. ^{88}Sr optical trap

The ^{88}Sr (stable, nat. abd. = 0.83, nuclear spin = 0) system of the optical lattice clock developed at JILA [27] is fully described in Refs. [28–31]. Here we focus only on the ^{88}Sr source and subsequent atomic beam, transverse cooler, Zeeman slower, and first-stage MOT, see Fig. 3. The atomic beam source is an effusive oven with a cylindrical nozzle of 0.2 cm diameter and 2 cm length. The crucible and nozzle temperatures are 525°C and 725°C , respectively. A 0.36 cm diameter filtering aperture located 19 cm downstream of the nozzle provides additional collimation.

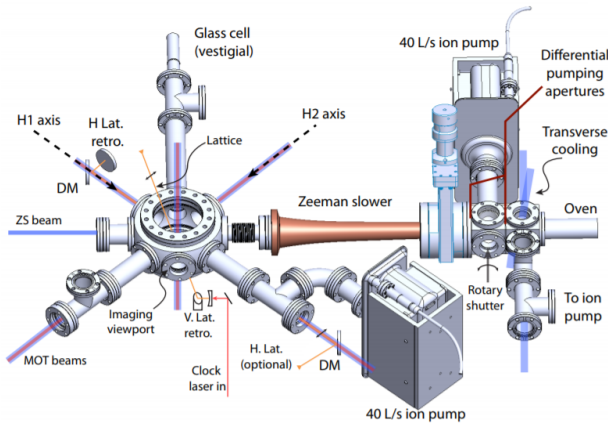


FIG. 3. The ^{88}Sr optical trapping apparatus. Figure from Ref. [31].

All laser-based interactions utilize the electric dipole transition $5s^2\ ^1S_0 \leftrightarrow 5s5p\ ^1P_1$ near 461 nm, see Fig. 1 (right), with a natural decay rate $\gamma_{\text{Sr}}/2\pi \approx 32 \text{ MHz}$ [28]. The first laser-atom interaction region is a transverse cooling region located shortly after the filtering aperture; this two-dimensional optical molasses is formed by

two orthogonal laser beams, each retro-reflected and elliptically shaped to have a long axis in the direction of atomic beam propagation, maximizing the interaction region. Next, the atomic beam passes through a gate valve and a shutter before entering the Zeeman slower. In this case, the slower is operated in a σ^- configuration [32], wherein the magnetic field increases with distance as the atom slows. This facilitates a sharp cutoff in the laser-atom interaction as the atom exits the slower. Here, the slower uses a peak magnetic field near 600 G to capture atoms with longitudinal velocities up to about 500 m s^{-1} . The Zeeman slower laser beam is assumed to be collimated with an intensity radius ($1/e^2$) of 0.2 cm and a saturation parameter of 12 near the center of the Gaussian beam¹ [33].

Parameter	Units	Sr expt.	Ra expt.
Cooling transition		$^1S_0 \leftrightarrow ^1P_1$	$^1S_0 \leftrightarrow ^3P_1$
Transition linewidth γ	MHz	32	0.38
Saturation intensity I_s	mW/cm^2	41	0.14
Transverse cooling intensity	I_s	0.3	120
Zeeman slower peak field	G	600	12
Zeeman slower detuning	γ	34	10
Zeeman slower intensity	I_s	12	80
MOT laser detuning	γ	1.3	6
MOT beam intensity	I_s	0.04	11
MOT B-field gradient	G/cm	50	1

TABLE I. Comparison of key parameters in the Sr and Ra experiments. All intensities are given as the peak intensity of the Gaussian beam, before retroreflection, and in units of the saturation intensity. All detunings are given in units of the transition linewidth.

After exiting the Zeeman slower, the slowed atoms are captured by a three-dimensional MOT. In the absence of repumping, the cold atoms eventually decay into the metastable “dark” state 3P_2 , with a 20 ms time constant. According to Ref. [28], the loading rate of the MOT is $2.7(9) \times 10^9$ atoms/s while the atomic flux after the filtering aperture is 3×10^{11} atoms/s, which gives the efficiency of the system (excluding the losses due to beam collimation from the filtering aperture) as $\eta_{\text{Sr,exp.}} = 9 \times 10^{-3}$. With two additional lasers to repump the atoms shelved in the long-lived 3P_2 state, the MOT lifetime is increased by a factor of 15 and becomes limited by collisions with the residual gas and/or

¹ Regarding the beam parameters used in the ^{88}Sr Zeeman slower, we note [33] that the beam shape is a distorted Gaussian, which when spatially-filtered gave nearly the same slowing efficiency despite having approximately half the total power. Thus we take the effective power as 30 mW.

the ^{88}Sr atomic beam, which passes directly through the MOT. See Tab. I for a summary of the key parameters for both experiments.

III. MONTE CARLO SIMULATION

In order to fully model the optical traps described in Sec. II, our MC simulation includes the main optical trapping subsystems (transverse cooler, Zeeman slower, and MOT) and as well as additional experimental details: the atomic beam source, gravity, laboratory magnetic fields, laser frequency noise, and residual gas collisions. We simulate the random walk of individual atoms in gravitational free-fall along the length of the modeled apparatus. The simulation outputs both the complete state of sampled atoms at each time step as well as the collective statistics of an entire simulation run (e.g. the overall trapping efficiency). The following subsections detail our implementation of these subsystems and processes.

A. Modelling the Atomic Beam Source

An effusive oven consists of a crucible and a collimating nozzle. These ovens operate in one of three flow regimes: molecular, intermediate, and viscous. These flow regimes determine the angular intensity and velocity distributions of the output atomic beam. The temperature of the crucible and geometry of the nozzle determine the flow regime of the oven, which is characterized by the Knudsen number,

$$\begin{aligned} K_{n_s} &= \frac{\lambda_{\text{atom}}}{d_{\text{noz}}} && \text{(short wide nozzle),} \\ K_{n_L} &= \frac{\lambda_{\text{atom}}}{L_{\text{noz}}} && \text{(long narrow nozzle),} \end{aligned} \quad (1)$$

where λ_{atom} is the mean free path of an atom in the oven, see Eq. B1 in appendix B, and d_{noz} and L_{noz} are the diameter and length of the nozzle, respectively. The aspect ratio of the nozzle,

$$\chi_{\text{AR}} = \frac{d_{\text{noz}}}{L_{\text{noz}}}, \quad (2)$$

characterizes the shape of the nozzle: $\chi_{\text{AR}} > 1$ for short wide nozzles and $\chi_{\text{AR}} < 1$ for long narrow nozzles. Both the Ra and Sr oven have long narrow nozzles, $\chi_{\text{AR}}(\text{Ra}) = 2.4 \times 10^{-2}$ and $\chi_{\text{AR}}(\text{Sr}) = 0.1$, and going forward we will refer to the Knudsen number as $K_n \equiv K_{n_L}$. For molecular flow ($K_n \gg 1$), the geometry of the nozzle determines the shape of the angular intensity distribution. In the intermediate flow ($K_n \approx 1$) regime, one must account for the influence that both interatomic collisions and the geometry of the nozzle have on the shape of the angular intensity distribution. For viscous flow ($K_n \ll 1$), hydrodynamic effects dominate the shaping of the angular intensity distribution and the

total flow rate from the oven. In molecular and intermediate flows, the velocity distribution of effusing atoms is a temperature-dependent Boltzmann distribution, perturbed by a Knudsen-number dependent factor for atoms with trajectories originating from the crucible (as opposed to a nozzle wall). See App. B for the formulation of the molecular and intermediate flow regime distributions; we do not consider viscous flow in the simulation.

We generate the angular intensity and velocity distributions from the geometry, temperature, and Knudsen number of the effusive oven in the optical trapping system we are modeling (e.g. the two optical traps described in Sec. II). A single atom is randomly placed within the area of the exit of the nozzle, and its trajectory is randomly sampled from the appropriate angular intensity distribution. We then project this trajectory backwards into the nozzle and crucible to determine the last wall with which the atom last came in contact. We assume the atom reaches thermal equilibrium before leaving this wall, so that the temperature of this wall sets the Boltzmann distribution from which we randomly sample the atom's velocity. Considering the crucible and nozzle temperatures separately allows simulation of temperature gradients in the oven.

B. Modeling Laser-Atom Interactions

The simulation models each laser field as a composition of circularly and linearly polarized laser beams. Each of these beams is defined by a reference point, propagation direction, transverse elliptical size, Gaussian intensity profile, divergence angle, polarization helicity, saturation intensity, and frequency detuning. We define two types of laser beams in the simulation: transition and repump beams. Each of these beams compete for the excitation of simulated atoms.

The transition beams operate on a defined atomic transition, which we treat as a two-level system with hyperfine splitting. We treat laser-atoms interactions semiclassically in the simulation: photon absorption and spontaneous emission follow electric dipole selection rules and angular distributions, and generate velocity kicks to the atom. Atoms reside in quantum states described by the total electronic angular momentum plus nuclear spin quantum number F and its projection m_F along the quantized axis, which we set along the direction of the external B-field. We assume that both F and m_F are conserved during ballistic flight and that stimulated emission is negligible. The total photon absorption rate is calculated by first determining the Zeeman shift of the m_F states caused by the local magnetic field, see Sec. III C below, and then summing over the Doppler-shift dependent saturation intensity of each beam. We take the photon absorption rate of any one laser beam as the total absorption rate weighted by the fractional saturation intensity contributed by that beam. See App. A for further details on the formulation of these rates.

We also include a stochastic noise process for transition beams such that the central frequency of a beam can undergo a random walk before being damped back to the central value. The noise is specified by an amplitude σ and damping time τ . The physical significance of the damping time can be, for example, a laser frequency servo loop with finite bandwidth, which in the Ra optical trap gives a damping time of $\tau = 50 \mu\text{s}$. The corresponding spectral density at each Fourier frequency f is white from D.C. to $f = 0.5/\tau$, after which it falls off like $1/f$.

We treat the repump beams and dark states more simply. Atoms in the excited state can decay to a metastable dark state. We model these dark states with a transition probability from the excited state and a characteristic lifetime that an atom will remain in the dark state. Multiple dark states are treated cumulatively and modeled as a single dark state with an overall transition probability and characteristic lifetime. If an atom is in a dark state and within the defined bounds of a repump laser beam, we return the atom to the ground state after a randomly-selected lifetime-weighted time step.

C. Magnetic Fields

Magnetic fields play a key role in modeling subsystems of an optical trapping apparatus, specifically the Zeeman slower and MOT. We include magnetic fields in the simulation from multiple sources: circular coil windings with specified current, ambient field maps, constant background fields, and a two-dimensional axisymmetric Zeeman slower. From these we calculate the total magnetic field as a three-dimensional grid of magnetic field vectors. The value of the local magnetic field is found by interpolating between points on this grid.

D. Collisions With Residual Gas Molecules

We consider the effect of collisions with residual gas molecules to simulate how a non-zero vacuum pressure alters an atom's trajectory in the simulation. Due to shallow trap depths, long-range dispersion forces in the form of induced dipole-dipole force $V = -C_6/R^6$ dominate the collisional cross section for ejection from a MOT, where C_6 is the long-range van der Waals coefficient and R is the intermolecular distance. To determine the collision frequency, scattering angle, and outgoing velocity, we first calculate the mean free path of the atom based on kinetic theory, from which we randomly determine the distance the atom travels before a collision. When a collision event occurs, we randomly sample the velocity of the residual gas molecule from a room-temperature Boltzmann distribution, and an impact parameter from a uniform distribution. Collisions with impact parameters beyond a specified cutoff value are ignored as we assume these lack the energy to significantly alter an atom's trajectory. With these values, and specified C_6 coefficients

and interaction distances, we numerically calculate the Lennard-Jones dynamics [34] to find the scattering angle and outgoing velocity, and update the atom's trajectory accordingly.

E. Simulating An Atom's Random Walk

We begin the simulation by generating an atom at the source oven as described in Sec. III A, see Fig. 4 (left). The atom will then proceed in a random walk through a series of time steps chosen based on the photon scattering and residual gas collision rates. All time steps are clamped to a specified maximum value. At the start of a time step, we calculate the photon absorption, spontaneous emission, repumping, and residual gas collision rates. Based on these rates, the shortest time step until the next event is chosen. We then update the atom's position and velocity accordingly while holding these rates constant. At the end of the time step, the process indicated by the rate the time step is chosen from is performed, and then a new iteration is started. We continue tracking an atom through these time steps until one of the following scenarios occur: the atom encounters a physical barrier (such as an aperture), leaves the defined bounds of the simulation, exceeds the specified total time limit, or becomes trapped in the MOT, see Fig. 4 (right). Finally, we terminate the simulation of that atom and update the lost and trapped atom counts accordingly.

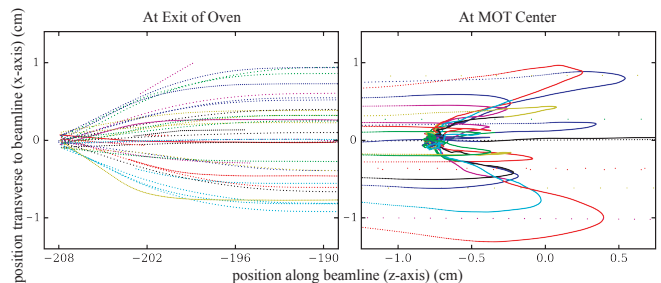


FIG. 4. Examples of atomic trajectories for the Radium Optical Trap. Note that the vertical scale is the same for both, but the horizontal scales are different.

F. Numerical Implementation

The simulation code consists of modules written in Fortran 90 and C, and we utilize the CERNLIB Programming Library [35] for numerical calculations. In order to parallelize our code, we use the Master/Slave algorithm implemented by the Asynchronous Dynamic Load Balancing (ADLB) Fortran interface [36, 37] to Message Passing Interface standard [38]. Using ADLB allows for work-sharing among a number of processors and computer nodes in a distributed-memory system. This permits rapid investigation of a large number of parameters

that affect the efficiency of the simulated optical traps.

IV. COMPARISON TO EXPERIMENT

In order to accurately model each of the optical traps described in Sec. II, we include all laser beams, known magnetic fields, and geometry using experimentally determined parameters. For each simulation, initial velocity and angular cuts discard atoms with velocity vectors that immediately leave the simulation bounds upon exiting the oven and atoms that have an initial velocity exceeding what the Zeeman slower can sufficiently slow. We minimize statistical errors in the simulation by simulating several thousand atoms within these angular and velocity cuts. In the Ra experiment we define the total efficiency as the ratio of the number of atoms trapped to the number of atoms exiting the source oven, as obtained by fluorescence measurements of the MOT and atomic beam, see Fig. 2. The ^{88}Sr efficiency definition differs in that the number of trapped atoms is compared to the number of atoms passing through the filtering aperture, not the total number exiting the oven.

We determine the simulated optical trapping efficiency in the same manner as the experimental value. The fluorescence measurements rely on limited knowledge of scattering rates, detector efficiencies, and detector solid angles, which results in roughly a factor of 3 uncertainty in the experimentally-determined overall trapping efficiencies. We expect that ratios of experimentally-determined trapping efficiencies to be more robust.

For the ^{88}Sr simulation, we use the experimental slowing beam parameters, see Sec. II B and Tab. I, and find a ^{88}Sr optical trapping efficiency of $\eta_{\text{Sr,sim}} = 4 \times 10^{-3}$. By adding transverse cooling, we see a four-fold increase in efficiency to $\eta_{\text{Sr,sim}} = 1.6 \times 10^{-2}$, which is in within a factor of 3 to the experimental value of $\eta_{\text{Sr,exp}} = 0.9 \times 10^{-2}$. Additionally, we find the trapping efficiency strongly depends on the slowing beam size and intensity. We observe that for a fixed optical power, we achieve optimal slowing using a central intensity of $4I_s$, and that increasing the beam size while maintaining this central intensity leads to higher trapping efficiency due to better overlap between the atomic and slowing laser beams. By expanding the slowing beam's intensity radius ($1/e^2$) to 0.4 cm, we further increase in the ^{88}Sr optical trapping efficiency by another factor of about 4.

For the ^{225}Ra simulation, we find a baseline optical trapping efficiency from slowing of the atomic beam of $\eta_{\text{Ra,sim}} = 4 \times 10^{-7}$. With the addition of both transverse cooling and repumping of the atomic beam, we find gains in efficiency of approximately 60 and 2.4, respectively, increasing the efficiency to $\eta_{\text{Sr,sim}} = 5.7 \times 10^{-5}$. This disagrees with the experimental value of $\eta_{\text{Ra,exp}} = 2 \times 10^{-6}$ by a factor of 30. Despite this discrepancy between the experimental and simulated total optical trapping efficiencies, we note the relatively good agreement on gain in efficiency produced by inclusion of the the trans-

verse cooling region and the 1428 nm repump laser (co-propagating with the slower laser). See Tab. II for a comparison of the experimental and simulated optical trapping efficiencies in the ^{88}Sr and ^{225}Ra optical traps.

	^{88}Sr exp.	^{88}Sr sim.	^{225}Ra exp.	^{225}Ra sim.
η , ZS only	2×10^{-3}	4×10^{-3}	1×10^{-8}	4×10^{-7}
TC gain	4	4	60	60
Repump gain	n/a	n/a	3.5	2.4
η , total	9×10^{-3}	1.6×10^{-2}	2×10^{-6}	5.7×10^{-5}

TABLE II. Comparison of ^{88}Sr and ^{225}Ra optical trapping efficiencies from experiment and simulation. (η : trapping efficiency; ZS: Zeeman slower; TC: transverse cooling) The systematic uncertainty in the experimentally determined total efficiencies is about a factor of 3. The statistical uncertainty in the simulated total efficiencies is about 5%.

V. SENSITIVITY STUDIES OF THE RADIUM OPTICAL TRAP

To diagnose the source of the discrepancy between the simulated and measured values of the ^{225}Ra optical trapping efficiency, we simulate possible systematic effects in the experiment that we did not originally account for in the simulation. The simulation's accurate prediction of relative gains in optical trapping efficiency allows for sensitivity studies to quantify the extent to which these systematic effects contribute to a reduced efficiency.

A. Influence of Residual Gas Inside the Oven

In both the experiment and simulation, we assume that the the dominant factor determining the mean free path of Ra is the saturated vapor pressure of Ba in the oven; all other known materials in the oven have vapor pressures significantly lower than Ba at the 500 °C operating temperature ($\text{SVP}_{\text{Ba}} = 138 \mu\text{Torr}$). This gives a mean free path of $\lambda_{\text{Ra}} \approx 42$ cm and Knudsen number $K_n \approx 5.1$, so we assume the oven operates in the intermediate flow regime. Any additional constituents within the oven with comparable (or higher) vapor pressures than Ba will reduce λ_{Ra} and broaden the angular distribution of the atomic beam exiting the oven. We fabricate the oven's crucible from Ti, which can absorb and store a significant amount of H_2 [39], so we cannot rule out the possibility that there is a significant H_2 partial pressure.

To characterize the impact that an increased H_2 partial pressure in the oven has on the optical trapping efficiency, we simulate a varying oven angular distribution by varying its Knudsen number from the oven's $K_n \approx 5.1$ down to the intermediate/viscous flow regime boundary at $K_n = \chi_{\text{AR}} = 2.4 \times 10^{-2}$. We do not consider the vis-

ous flow regime in our simulation. From the results of these simulations, see Fig. 5, we find that it takes a H_2 partial pressure in the oven $> 1 \times 10^{-3}$ Torr ($K_n \approx 1$) to see a significant decrease in the optical trapping efficiency below our initial results using only Ba to determine the oven's angular distribution. For H_2 in the oven to significantly contribute to the discrepancy between measured and simulated trapping efficiencies, a partial pressure $\gg 2$ mTorr is required, which may be possible due to differential pumping given the conductance of the oven nozzle. Without means to directly measure the pressure in the oven, we cannot rule out the influence of residual gas inside the oven as a contribution to the discrepancy between the measured and simulated optical trapping efficiencies.

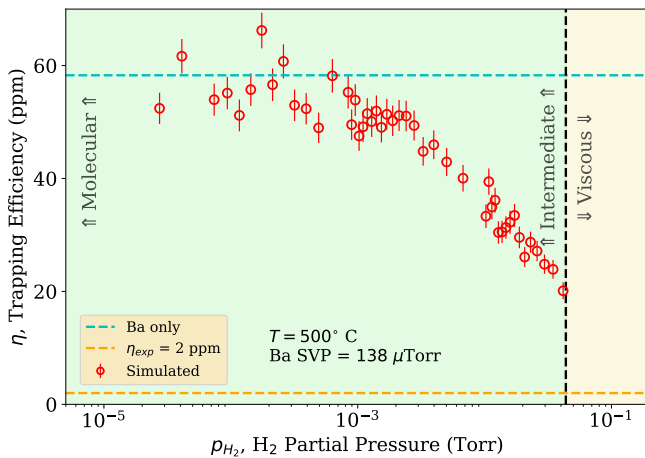


FIG. 5. The influence of H_2 partial pressure in the oven on the optical trapping efficiency. Data points represent a varying H_2 partial pressure and a constant Ba partial pressure of $138 \mu\text{Torr}$ at an oven temperature of 500°C . The optical trapping efficiency remains unchanged until reaching a H_2 partial pressure of about 3×10^{-4} Torr, approximately a Knudsen number of $K_n \approx 2$ which is well within the bounds of the intermediate flow regime.

B. Misaligned Oven Nozzle

A misalignment between the oven nozzle and Zeeman slower axis potentially reduces the optical trapping efficiency. We can partially correct for this in the experiment by carefully realigning the transverse cooling beams. To model these misalignments in the simulation, we rotate and translate the oven nozzle off the Zeeman slower axis. From mechanical constraints, we bound these misalignments to $\pm 10^\circ$ and ± 1 cm, respectively. For these studies we do not modify the properties of the transverse cooler to correct for the induced misalignments. The results, see Fig. 6, show that small misalignments of the nozzle do not alone cause the factor of 30 discrepancy in trapping efficiency with the experimental results, although we cannot rule out a small contribution.

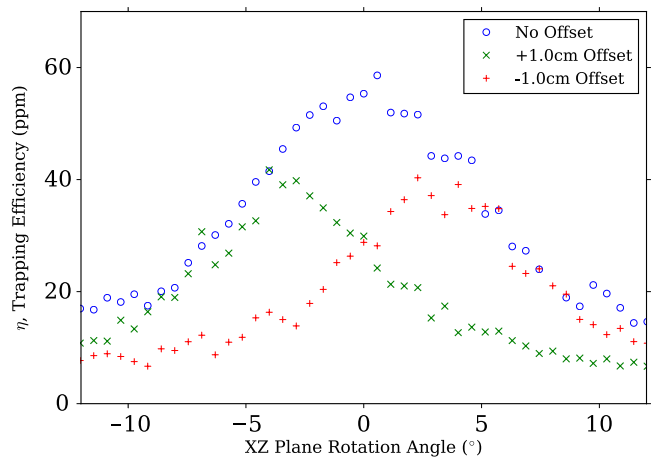


FIG. 6. Simulated optical trapping efficiency with oven nozzle misalignments. Rotations and offsets are in the XZ-plane where the Zeeman slower is aligned along the Z-axis.

C. Influence of Residual Gas Outside the Oven

To test the effect of a non-zero vacuum pressure in the transverse cooling region, we simulate collisions between Ra and a residual gas of H_2 . With estimates for the C_6 coefficients and bond lengths as described in App. C, we find that our baseline vacuum pressure (3×10^{-7} Torr) reduces the ^{225}Ra optical trapping efficiency by a factor of 1.4 when compared to the collision-free scenario. Increasing the pressure in the transverse cooling region by a factor of 10 further reduces the efficiency by a factor of 1.9, see Fig. 7. These results suggest that the ^{225}Ra optical trapping efficiency is only weakly sensitive to residual gas collisions in the transverse cooling region, which may indicate that low impact collisions can be corrected for with optical forces. We also simulated the MOT with our residual gas collision model and determined a MOT trap lifetime of 15 s which agrees with the experimentally determined value at a residual gas pressure of 10^{-9} Torr to better than a factor of two.

D. Stray Magnetic Fields in the Transverse Cooler

We include all known magnetic sources in the simulation, including the Zeeman slower, MOT coils, and the uniform contribution from the earth's magnetic field as measured in the laboratory. We do not explicitly include stray magnetic fields, such as those from ion pump magnets and high current heating elements in the oven. In order to test the effect that these stray fields have on the trapping efficiency, we model magnetic fields in the transverse cooling region by adding fictitious coils and varying their orientation and magnetic strength. The results of these simulations, see Fig. 8, show that a stray magnetic field of magnitude in excess of 1 G is required to significantly reduce the optical trapping efficiency to

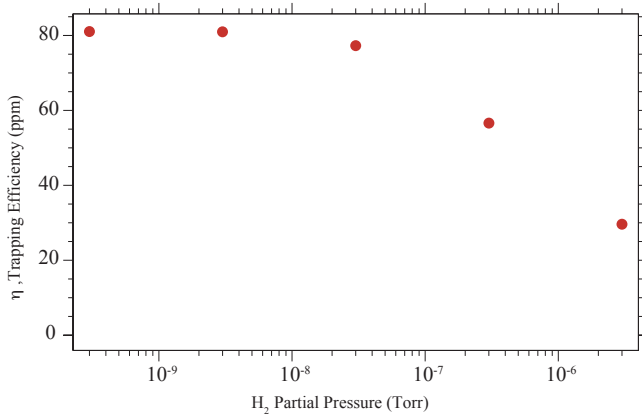


FIG. 7. The influence of vacuum pressure in the transverse cooling region on the optical trapping efficiency. Data points represent a varying H₂ number density at room temperature.

the levels measured in the apparatus. Furthermore, in order to test the predictions of the simulation results, we added rectangular coils in the TC region and experimentally measured the change in the atomic fluorescence from the MOT as a function of applied magnetic field in the TC region using ²²⁶Ra as a surrogate for ²²⁵Ra. The measured results qualitatively agree with the simulation, namely a stray field of in excess of 1 G is needed to significantly lower the trapping efficiency. We do not expect uncontrolled fields of this magnitude within the Ra optical trap so we do not expect these stray magnetic fields to be a major contributor to the discrepancy between the measured and simulated optical trapping efficiencies.

E. Laser Frequency Noise

In the Ra optical trap, we generate the 714 nm light with a Ti:sapphire ring laser referenced to a high-finesse optical cavity. The resulting laser spectrum is mostly white with a few peaks in the kHz range, and we measure the overall linewidth to be approximately 100 kHz $\approx 0.3 \gamma_{\text{Ra}}$. We simulate potential noise sources by varying the noise amplitude and damping time associated with individual laser beams. Based on the results of these simulations, see Fig. 9, we do not expect the ²²⁵Ra optical trapping efficiency to be limited by laser linewidth and frequency noise.

F. MOT Beam Misalignment and Imbalance

We trap Ra atoms using a 3D MOT created by a quadrupole magnet and three orthogonal laser beams of the appropriate helicity intersecting where the magnetic field goes to zero. These beams are retroreflected outside of the vacuum chamber. We measured the optical losses due to reflections from the vacuum viewports and found

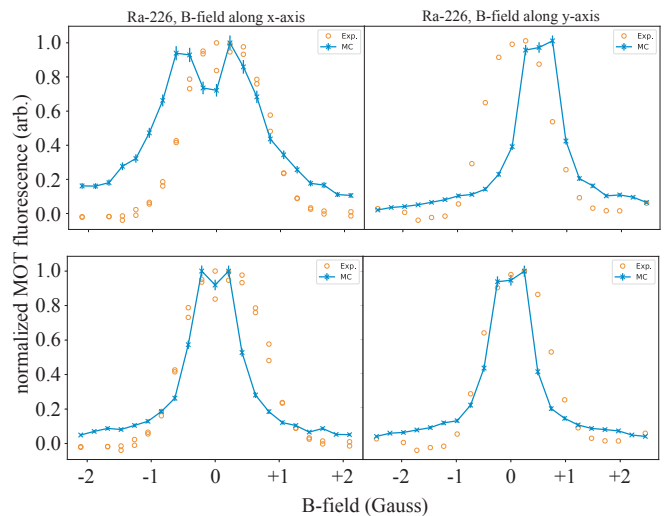


FIG. 8. The influence of stray magnetic fields on the ²²⁶Ra optical trapping efficiency. Fields are simulated with coil windings placed along each of the coordinate axes in the transverse cooling region with varying values of current. The shifts in the peak efficiency are, shown in the upper two plots, are due to the Earth’s magnetic field in the simulation, which is “tuned out” in the experimental setup. The bottom two plots show the efficiencies when the Earth’s magnetic field is “turned off” in the simulation.

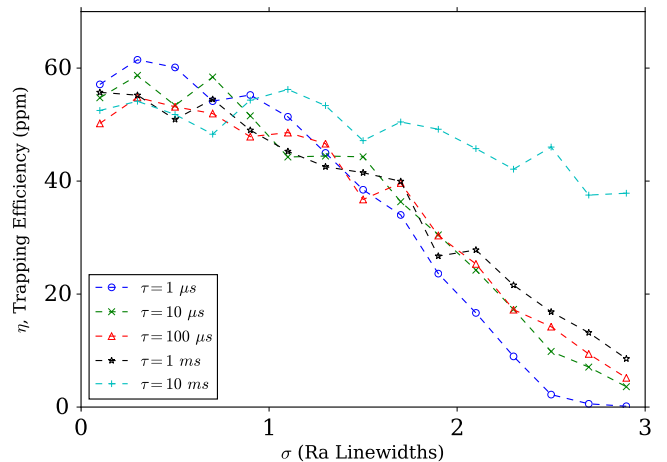


FIG. 9. The influence of laser frequency noise on the ²²⁵Ra optical trapping efficiency. The horizontal axis (σ) is the laser linewidth in terms of the Ra atomic linewidth. The different curves correspond to different values of the damping time τ .

that the retroreflected beams have 10% less power than their forward-going counterparts. These six laser beams are modelled as three intensity-imbalanced orthogonal pairs of anti-parallel and opposite helicity beams. In the simulation, this imbalance produces a small shift in the position of the MOT’s center, but no change in the trapping efficiency is observed. Further increases to the intensity imbalance between pairs of retroreflected beams

likewise shifted the MOT center while leaving the trapping efficiency unchanged. This agrees with our assumption that the MOT operates at a very high saturation parameter, lessening the effect of small changes in the global intensity on the optical trapping efficiency.

While ensuring anti-parallelism between each MOT beam and its retroreflection is relatively straightforward experimentally, it is more difficult to ensure that the global overlap of the three beams is optimal. We tested the impact of sub-optimal MOT beam overlap in the simulation by individually offsetting one pair of beams from the others. Generally speaking, displacements of up to 1 cm (approximately the intensity radius of the MOT beams) produces no significant losses in the optical trapping efficiency, and we do not expect misalignments in the experiment to be any larger than this.

VI. SUMMARY & CONCLUSIONS

We have presented a three-dimensional MC simulation of an optical trapping apparatus that includes the effects of several common perturbations to the laser cooling and trapping process. With this simulation we model the optical trapping apparatus used in our ^{225}Ra EDM measurements in an effort to improve our optical trapping efficiency of ^{225}Ra . Our simulation mostly agrees with the experimental results of both the ^{225}Ra and ^{88}Sr optical trapping systems, i.e. we see the same relative gains in trapping efficiency from switching on/off components of the apparatus, and we find good agreement between the measured and simulated ^{88}Sr optical trapping efficiencies. However, the ^{225}Ra simulation results differ from experimental results by a factor of 30. We note that we may not see the discrepancy between measured and simulated trapping efficiencies in the ^{88}Sr optical trap since we do not consider the full trapping efficiency in the system. Simulations of possible systematic effects in the apparatus so far have shown that there is no sole-source of this discrepancy, but rather these effects may cumulatively explain this difference between the measured and simulated trapping efficiencies.

In addition to these systematic effects, potential contributions to this discrepancy may result from other aspects of our simulation. For example, our treatment of the effusive-oven atomic beam source may not be ade-

quate for the complex chemistry in the Ra oven. We plan on determining the adequacy of this atomic beam source model by detailed study of the output of effusive ovens with chemical surrogates for Ra (such as Ca) in comparison to the simulation's predictions.

While a discrepancy exists between the measured and simulated optical trapping efficiencies, the accurate relative gains predicted by the simulation for both the Ra and ^{88}Sr optical traps makes this simulation a valuable tool for studying and optimizing the optical trapping of rare isotopes. In the case of the ^{225}Ra optical trap, we plan to use the simulation to test and optimize and a planned “blue slower” upgrade. Our present “red-slowing” scheme ($^1S_0 \leftrightarrow ^3P_1$ near 714 nm) can only slow and trap atoms with initial velocities of up to 63 m s^{-1} , approximately $< 0.5\%$ of the oven's velocity distribution. The blue-slower upgrade will use the stronger $^1S_0 \leftrightarrow ^1P_1$ transition near 483 nm, allowing us to slow and trap atoms with initial velocities of up to 310 m s^{-1} , approximately 50% of the oven's velocity distribution. Implementing this scheme will require frequency chirping of the slowing laser and additional repump lasers to handle the additional atomic dark states associated with this transition. We plan on upgrading the simulation to include both frequency chirping and additional repumping transitions, and using the upgraded simulation to help implement and optimize the blue slower in the ^{225}Ra optical trap. This upgrade to the ^{225}Ra optical trap will offer increased EDM measurement precision by increasing our optical trapping efficiency by up to two orders of magnitude.

ACKNOWLEDGMENTS

The authors wish to thank A. Ludlow for helpful discussions regarding the ^{88}Sr apparatus. This work is supported by the U.S. DOE, Office of Science, Office of Nuclear Physics under contracts DE-AC02-06CH11357 and de-sc0019455, the Director's Research Scholars Program at the National Superconducting Cyclotron Laboratory, and by Michigan State University through computational resources provided by the Institute for Cyber-Enabled Research. SAF acknowledges support from the United States Department of Energy through the Computational Science Graduate Fellowship, grant number de-sc0019323.

-
- [1] N. C. Sturchio, X. Du, R. Purtschert, B. E. Lehmann, M. Sultan, L. J. Patterson, Z.-T. Lu, P. Mueller, T. Bigler, K. Bailey, T. P. O'Connor, L. Young, R. Lorenzo, R. Becker, Z. El Alfy, B. El Kaliouby, Y. Dawood, and A. M. A. Abdallah, *Geophysical Research Letters* **31** (2004), 10.1029/2003GL019234.
- [2] W. Jiang, W. Williams, K. Bailey, A. M. Davis, S.-M. Hu, Z.-T. Lu, T. P. O'Connor, R. Purtschert, N. C. Sturchio,

- Y. R. Sun, and P. Mueller, *Phys. Rev. Lett.* **106**, 103001 (2011).
- [3] Z.-T. Lu, P. Mueller, G. W. F. Drake, W. Nörtershäuser, S. C. Pieper, and Z.-C. Yan, *Rev. Mod. Phys.* **85**, 1383 (2013).
- [4] P. Mueller, I. A. Sulai, A. C. C. Villari, J. A. Alcántara-Núñez, R. Alves-Condé, K. Bailey, G. W. F. Drake, M. Dubois, C. Eléon, G. Gaubert, R. J. Holt, R. V. F.

- Janssens, N. Lecesne, Z.-T. Lu, T. P. O'Connor, M.-G. Saint-Laurent, J.-C. Thomas, and L.-B. Wang, *Phys. Rev. Lett.* **99**, 252501 (2007).
- [5] L.-B. Wang, P. Mueller, K. Bailey, G. W. F. Drake, J. P. Greene, D. Henderson, R. J. Holt, R. V. F. Janssens, C. L. Jiang, Z.-T. Lu, T. P. O'Connor, R. C. Pardo, K. E. Rehm, J. P. Schiffer, and X. D. Tang, *Phys. Rev. Lett.* **93**, 142501 (2004).
- [6] P. A. Vetter, J. R. Abo-Shaer, S. J. Freedman, and R. Maruyama, *Phys. Rev. C* **77**, 035502 (2008).
- [7] B. Fenker, A. Gorelov, D. Melconian, J. A. Behr, M. Anholm, D. Ashery, R. S. Behling, I. Cohen, I. Craiciu, G. Gwinner, J. McNeil, M. Mehlman, K. Olchanski, P. D. Shidling, S. Smale, and C. L. Warner, *Phys. Rev. Lett.* **120**, 062502 (2018).
- [8] M. Gonzalez-Alonso, O. Naviliat-Cuncic, and N. Severijns, *Progress in Particle and Nuclear Physics* **104**, 165 (2019).
- [9] M. Tandecki, J. Zhang, R. Collister, S. Aubin, J. A. Behr, E. Gomez, G. Gwinner, L. A. Orozco, and M. R. Pearson, *J. Instrum.* **8**, P12006 (2013), arXiv:1312.3562 [physics.atom-ph].
- [10] R. H. Parker, M. R. Dietrich, K. Bailey, J. P. Greene, R. J. Holt, M. R. Kalita, W. Korsch, Z.-T. Lu, P. Mueller, T. P. O'Connor, J. Singh, I. A. Sulai, and W. L. Trimble, *Phys. Rev. C* **86**, 065503 (2012).
- [11] T. E. Chupp, P. Fierlinger, M. J. Ramsey-Musolf, and J. T. Singh, *Rev. Mod. Phys.* **91**, 015001 (2019).
- [12] N. Auerbach, V. V. Flambaum, and V. Spevak, *Phys. Rev. Lett.* **76**, 4316 (1996).
- [13] J. Dobaczewski and J. Engel, *Phys. Rev. Lett.* **94**, 232502 (2005).
- [14] M. Bishof, R. H. Parker, K. G. Bailey, J. P. Greene, R. J. Holt, M. R. Kalita, W. Korsch, N. D. Lemke, Z.-T. Lu, P. Mueller, T. P. O'Connor, J. T. Singh, and M. R. Dietrich, *Phys. Rev. C* **94**, 025501 (2016).
- [15] R. Blatt, W. Ertmer, P. Zoller, and J. L. Hall, *Phys. Rev. A* **34**, 3022 (1986).
- [16] J. Javanainen, *Phys. Rev. A* **46**, 5819 (1992).
- [17] E. J. D. Vredenburg and K. A. H. van Leeuwen, *Am. J. Phys.* **71**, 760 (2003).
- [18] M. Hamamda, T. Taillandier-Loize, J. Baudon, G. Dutier, F. Perales, and M. Ducloy, *Eur. Phys. J. Appl. Phys.* **71**, 30502 (2015).
- [19] Y. Castin and K. Mølmer, *Phys Rev Lett* **74**, 3772 (1995).
- [20] J. W. Dunn and C. H. Greene, *Phys. Rev. A* **73**, 033421 (2006).
- [21] W. C. Griffith, M. D. Swallows, T. H. Loftus, M. V. Romalis, B. R. Heckel, and E. N. Fortson, *Phys. Rev. Lett.* **102**, 101601 (2009).
- [22] R. Holt, I. Ahmad, K. Bailey, B. Graner, J. Greene, *et al.*, *Nucl. Phys.* **A844**, 53c (2010).
- [23] J. R. Guest, N. D. Scielzo, I. Ahmad, K. Bailey, J. P. Greene, R. J. Holt, Z.-T. Lu, T. P. O'Connor, and D. H. Potterveld, *Phys. Rev. Lett.* **98**, 093001 (2007).
- [24] R. H. Parker, M. R. Dietrich, M. R. Kalita, N. D. Lemke, K. G. Bailey, M. Bishof, J. P. Greene, R. J. Holt, W. Korsch, Z.-T. Lu, P. Mueller, T. P. O'Connor, and J. T. Singh, *Phys. Rev. Lett.* **114**, 233002 (2015).
- [25] G. Breit and L. A. Wills, *Phys. Rev.* **44**, 470 (1933).
- [26] N. D. Scielzo, J. R. Guest, E. C. Schulte, I. Ahmad, K. Bailey, D. L. Bowers, R. J. Holt, Z.-T. Lu, T. P. O'Connor, and D. H. Potterveld, *Phys. Rev. A* **73**, 010501(R) (2006).
- [27] A. D. Ludlow, T. Zelevinsky, G. K. Campbell, S. Blatt, M. M. Boyd, M. H. G. de Miranda, M. J. Martin, J. W. Thomsen, S. M. Foreman, J. Ye, T. M. Fortier, J. E. Stalnaker, S. A. Diddams, Y. Le Coq, Z. W. Barber, N. Poli, N. D. Lemke, K. M. Beck, and C. W. Oates, *Science* **319**, 1805 (2008).
- [28] T. H. Loftus, T. Ido, M. M. Boyd, A. D. Ludlow, and J. Ye, *Phys. Rev. A* **70**, 063413 (2004).
- [29] A. D. Ludlow, *The strontium optical lattice clock: optical spectroscopy with sub-hertz accuracy*, Ph.D. thesis, University of Colorado-Boulder (2008).
- [30] M. M. Boyd, *High Precision Spectroscopy of Strontium in an Optical Lattice: Towards a New Standard for Frequency and Time*, Ph.D. thesis, University of Colorado-Boulder (2007).
- [31] M. J. Martin, *Quantum Metrology and Many-Body Physics: Pushing the Frontier of the Optical Lattice Clock*, Ph.D. thesis, University of Colorado-Boulder (2013).
- [32] T. E. Barrett, S. W. Daport-Schwartz, M. D. Ray, and G. P. Lafyatis, *Phys. Rev. Lett.* **67**, 3483 (1991).
- [33] A. Ludlow, "Private communication," (2013).
- [34] A. Venkattraman and A. A. Alexeenko, *Phys. Fluids* **24**, 027101 (2012).
- [35] C. P. Libary, K. Kölbig, E. O. for Nuclear Research. Computing, and N. D. A. S. Group, *CERNLIB: Short Writeups* (CERN, 1993).
- [36] S. Bogner, A. Bulgac, J. A. Carlson, J. Engel, G. Fann, *et al.*, *Comput. Phys. Commun.* **184**, 2235 (2013), arXiv:1304.3713 [nucl-th].
- [37] E. L. Lusk, S. C. Pieper, and R. M. Butler, *SciDac Rev. B* **17**, 30 (2010).
- [38] T. M. Forum, "Mpi: A message passing interface," (1993).
- [39] T. Yildirim and S. Ciraci, *Phys. Rev. Lett.* **94**, 175501 (2005).
- [40] B. W. Shore, *The Theory of Coherent Atomic Excitation, Volume 2, Multilevel Atoms and Incoherence* (Wiley-VCH, 1990).
- [41] H. Metcalf and P. van der Straten, *Laser Cooling and Trapping*, Graduate Texts in Contemporary Physics (Springer New York, 2001).
- [42] J. Rumble, ed., *CRC Handbook of Chemistry and Physics, 98th Edition* (CRC Press, 2017).
- [43] G. Scoles, ed., *Atomic and Molecular Beam Methods : Volume 1 (Atomic & Molecular Beam Methods)* (Oxford University Press, USA, 1988).
- [44] D. R. Olander and V. Kruger, *Journal of Applied Physics* **41**, 2769 (1970).
- [45] D. Olander, R. Jones, and W. Siekhaus, *Journal of Applied Physics* **41**, 4388 (1970).
- [46] T. Arpornthip, C. A. Sackett, and K. J. Hughes, *Phys. Rev. A* **85**, 033420 (2012).
- [47] T. Q. Teodoro, R. L. A. Haiduke, U. Dammalapati, S. Knoop, and L. Visscher, *The Journal of Chemical Physics* **143**, 084307 (2015).
- [48] S. Porsev and A. Derevianko, *J. Exp. Theor. Phys.* **102**, 195 (2006).
- [49] I. F. Silvera and V. V. Goldman, *The Journal of Chemical Physics* **69**, 4209 (1978).
- [50] C. Bissonnette, C. E. Chuaqui, K. G. Crowell, R. J. L. Roy, R. J. Wheatley, and W. J. Meath, *The Journal of Chemical Physics* **105**, 2639 (1996).
- [51] R. A. Aziz and H. H. Chen, *The Journal of Chemical*

Appendix A: Calculation of photon absorption rates

We decompose the laser field into an array of circularly and linearly polarized beams, all of which compete for the excitation of the atom. The beams are described by a reference point \vec{x} , a propagation direction \vec{p} , transverse elliptical size (r_1, r_2) , Gaussian intensity profile (σ_1, σ_2) , divergence angle (d_1, d_2) , polarization helicity ($h = \pm 1$ for circularly polarized and $h = 0$ for linearly polarized), saturation intensity $\beta = I/I_{\text{sat}}$ and detuning $\Gamma = \delta/\gamma$ where δ is the bare laser detuning and $\gamma = 1/\tau$ is the natural linewidth with τ the upper state lifetime.

We determine the intensity β_i and photon direction \vec{p}_i of each beam (indicated by the subscript i) at the location of the atom. The Zeeman shift of the upper (lower) state in natural linewidths per unit m_F is [40]:

$$Z_{u(l)} = \frac{\mu_B g_{u(l)}}{\hbar} B \tau \quad (\text{A1})$$

where μ_B is the Bohr magneton and \hbar the reduced Planck constant, $g_{u(l)}$ is the Landè g-factor of the upper (lower) state, τ is the natural lifetime of the upper state, and $B \equiv |\vec{B}|$ is the magnetic field amplitude.

The Doppler shift D_i in natural linewidths is given by:

$$D_u = -2\pi \frac{\tau}{\lambda} \vec{v} \cdot \vec{p}_i \quad (\text{A2})$$

where \vec{v} is the velocity of the atom and λ is the wavelength of the photon.

The angular distribution for the transition probability [40] $W_{i,\Delta m}$ for circularly polarized light ($h = \pm 1$) is:

$$\begin{aligned} W_{i,1} &= \frac{1}{4}(1 + h \cos(\theta_i))^2 \\ W_{i,0} &= \frac{1}{2} \sin^2(\theta_i) \\ W_{i,-1} &= \frac{1}{4}(1 - h \cos(\theta_i))^2 \end{aligned} \quad (\text{A3})$$

and for linearly polarized light ($h = 0$) by:

$$\begin{aligned} W_{i,1} &= \frac{1}{2} \cos^2(\theta_i) \\ W_{i,0} &= \sin^2(\theta_i) \\ W_{i,-1} &= \frac{1}{2} \cos^2(\theta_i) \end{aligned} \quad (\text{A4})$$

where θ_i is the angle between \vec{B} and \vec{p}_i , and $\Delta m = 0, \pm 1$ is the change in m_F for the transition. We treat all linear polarization as vertical since there is no preferred direction orthogonal to \vec{p}_i in the frame of the laser beam. We sum over the contributions of $W_{i,\Delta m}$ to find the effective intensity of each laser i :

$$\begin{aligned} \beta'_i &= \sum_{\Delta m=-1}^1 \beta'_{i,\Delta m} \\ &= \sum_{\Delta m=-1}^1 \frac{\beta_i W_{i,\Delta m}}{1 + 4[\Gamma_i + D_i + m_F Z_l - (m_F + \Delta m) Z_u]^2} \end{aligned} \quad (\text{A5})$$

We model a non-zero laser linewidth by re-defining the saturation parameter β as

$$\beta = \beta_0 \int_{-\infty}^{\infty} \frac{L(x) dx}{1 + 4(x + \Gamma)^2} \quad (\text{A6})$$

where $\beta_0 = I/I_{\text{sat}}$ is the on-resonance saturation parameter, $L(x)$ is a normalized Lorentzian function, and $\Gamma = \delta/\gamma_{\text{Ra}}$ is the detuning. Evaluating the integral we find

$$\frac{\beta}{\beta_0} = \frac{1 + w}{4\Gamma^2 + (1 + w)^2} \quad (\text{A7})$$

where w is the full-width at half-maximum of the Lorentzian. In the limit $w \rightarrow 0$, we recover the familiar definition of the saturation parameter [41]. This effectively broadens the absorption spectrum, leading to increased excitation probability at large detuning, but reduced excitation probability close to resonance.

The total absorption rate (R_T) and fractional absorption rate ($R_{i,\Delta m}$) for each beam i are:

$$\begin{aligned} R_T &= \frac{\beta'_T}{(2 + \beta'_T)\tau} \\ R_{i,\Delta m} &= R_T \left(\frac{\beta'_{i,\Delta m}}{\beta'_T} \right) \end{aligned} \quad (\text{A8})$$

where $\beta'_T = \sum_i \beta'_i$ is the total intensity. We emphasize that this is the photon absorption rate for the ground state of the atom; once the atom is excited, we set the absorption rate to zero and the emission rate to γ , ignoring stimulated emission.

Appendix B: Effusive oven velocity and angular distributions

For an an effusive oven with a Knudsen number $K_n = \lambda_{\text{atom}}/L_{\text{noz}}$, we calculate the mean free path of the atom:

$$\lambda_{\text{atom}} = \frac{k_b T}{\sqrt{2\pi} d^2 P} \quad (\text{B1})$$

where k_B is the Boltzmann constant, T is the temperature, d is the interaction distance between two atoms (taken as the sum of the van der Waals radii), and P is the saturated vapor pressure at a temperature T , calculated as [42]:

$$\log_{10} \left(\frac{P}{X} \right) = A + \frac{B}{T} + C \log_{10} T + \frac{D}{T^3} \quad (\text{B2})$$

where X is the pressure per atmosphere in the desired units, and A , B , C , and D are experimentally obtained coefficients available in Ref. [42].

We determine the velocity distribution of the atoms in the simulation by the temperature T of the last wall in the oven or nozzle that an atom collides with as [43–45]:

$$f(u) = A[f_{\text{beam}}(u)\mathcal{P}(K_n, \psi(u))] \quad (\text{B3})$$

where u is the reduced velocity v_z/\tilde{v} (v_z is the longitudinal component of the velocity) and $\tilde{v} \equiv \sqrt{2k_B T/M}$ is the most probable velocity where M the mass of the atom. A is a normalization constant satisfying $\int_0^\infty f(u) du = 1$. The unperturbed Boltzmann distribution for an atomic beam is:

$$f_{\text{beam}}(u) = \frac{2u^3}{\tilde{v}} \exp(-u^2) \quad (\text{B4})$$

and the Knudsen number perturbation is:

$$\mathcal{P}(K_n, \psi(u)) = \frac{\sqrt{\pi} \operatorname{erf} \sqrt{\psi(u)/2K_n}}{2} \frac{\sqrt{\psi(u)/2K_n}}{\sqrt{\psi(u)/2K_n}} \quad (\text{B5})$$

with the function $\psi(u)$ defined as:

$$\psi(u) = \frac{ue^{-u^2} + (\sqrt{\pi}/2)(1 + 2u^2) \operatorname{erf}(u)}{\sqrt{2\pi}u^2} \quad (\text{B6})$$

We include both the molecular and intermediate flow regime distributions in the simulation and reproduce the formulas from Refs. [43, 44] below. The molecular flow angular distribution depends solely on the oven nozzle's geometry, and for polar angles θ from the axis of the atomic beam, the distribution of angles originating from the oven ($\chi_{\text{AR}} \geq \tan \theta$ where $\chi_{\text{AR}} = d_{\text{noz}}/L_{\text{noz}}$) is:

$$j_{\mathcal{M}}(\theta) = \zeta_0 \cos \theta + \frac{2}{\pi} [(1 - \zeta_0)R(q)] \cos \theta + \frac{4}{3\pi q} [1 - (1 - q^2)^{3/2}] [\zeta_1 - \zeta_0] \cos \theta \quad (\text{B7})$$

and for angles originating from the nozzle wall ($\chi_{\text{AR}} \leq \tan \theta$):

$$j_{\mathcal{M}}(\theta) = \zeta_0 \cos \theta + \frac{4}{3\pi q} (\zeta_1 - \zeta_0) \cos \theta \quad (\text{B8})$$

where the following definitions are used:

$$q = \tan \theta / \chi_{\text{AR}} \quad (\text{B9})$$

$$R(q) = \cos^{-1}(q) - q\sqrt{1 - q^2} \quad (\text{B10})$$

and the collision rates with the nozzle walls at the exit and entrance, ζ_0 and ζ_1 , respectively, are two dimensionless parameters defined as:

$$\zeta_0 = \zeta_1 - \frac{(1 + 2/\chi_{\text{AR}})\sqrt{1 + 1/\chi_{\text{AR}}^2} - (1 + 2/\chi_{\text{AR}}^2)}{\sqrt{1 + 1/\chi_{\text{AR}}^2} + 1} \quad (\text{B11})$$

$$\zeta_1 = [1 + \chi_{\text{AR}}/(2 + \chi_{\text{AR}}^2)]^{-1}$$

The intermediate flow regime angular distribution accounts for both the nozzle's geometry and interatomic collisions in the nozzle. This distribution depends on the Knudsen number as well as the number density of the atoms at the exit and entrance of the nozzle, characterized by the two dimensionless parameters ζ_0 and ζ_1 ,

which are conventionally defined as $\xi_0 \equiv \zeta_0$ and $\xi_1 \equiv \zeta_1$. The distribution for $\chi_{\text{AR}} \geq \tan \theta$ is:

$$j_{\mathcal{I}}(\theta) = \xi_0 \cos \theta \left[1 + \frac{2}{\sqrt{\pi}} \frac{e^{\delta'^2}}{\delta'} S(q) \right] + \frac{\xi_0 \cos \theta e^{\delta'^2}}{\sqrt{\pi}} \frac{1}{\delta'} \left[R(q) \left(\operatorname{erf} \xi' - \operatorname{erf} \delta' + F(\xi_0, \xi_1, \delta') \right) \right] \quad (\text{B12})$$

and for $\chi_{\text{AR}} \leq \tan \theta$:

$$j_{\mathcal{I}}(\theta) = \xi_0 \cos \theta \left[1 + \frac{2}{\sqrt{\pi}} \frac{e^{\delta'^2}}{\delta'} S(1) \right] \quad (\text{B13})$$

and at $\theta = 0$:

$$j_{\mathcal{I}}(0) = \xi_0 + \frac{\sqrt{\pi}}{2} \xi_0 \frac{e^{\delta^2}}{\delta} \left(\operatorname{erf} \xi - \operatorname{erf} \delta \right) + \left(\frac{1 - \xi_1}{\xi_0} \right) e^{-(\xi^2 - \delta^2)} \quad (\text{B14})$$

where the following definitions are used:

$$\delta = \sqrt{\frac{\xi_0^2}{2K_n(\xi_1 - \xi_0)}} \quad , \quad \xi = \left(\frac{\xi_1}{\xi_0} \right) \delta \quad (\text{B15})$$

$$\delta' = \sqrt{\frac{\delta^2}{\cos \theta}} \quad , \quad \xi' = \left(\frac{\xi_1}{\xi_0} \right) \delta' \quad (\text{B16})$$

$$F(\xi_0, \xi_1, \delta') = \frac{2}{\sqrt{\pi}} \xi' \left(\frac{1}{\xi_1} - 1 \right) e^{-\xi'^2} \quad (\text{B17})$$

$$S(q) = \int_0^q dz \sqrt{1 - z^2} \times \left(\operatorname{erf} \left\{ \delta' \left[1 + \frac{z}{q} \left(\frac{\xi_1}{\xi_0} - 1 \right) \right] \right\} - \operatorname{erf} \delta' \right) \quad (\text{B18})$$

Appendix C: Estimate of long-range van der Waals C_6 coefficients

Residual gas collisions alter an atom's trajectory and can eject atoms from the MOT. To assess the impact of these effects on the optical trapping efficiency, we included a non-zero residual gas pressure in the simulation. For relevant residual gases in the ^{225}Ra optical trap, e.g. H_2 and Ar , no data exists for the C_6 coefficient with Ra . Instead, we estimate the coefficients with the London dispersion formula:

$$C_6 = \frac{3}{2} \left(\frac{U_1 U_2}{U_1 + U_2} \right) \alpha_1 \alpha_2 \quad (\text{C1})$$

where α_i is the polarizability (in \AA^3) and U_i a relevant energy scale for each constituent. For tightly bound species such as molecules and noble gases, we estimate U_i as the ionization energy, whereas for alkaline earths, such as Ra and Ba, we estimate U_i as the energy of the $^1S_0 \rightarrow ^1P_1$ transition, as this state dominates the ground state polarizability. We then calculate a table of C_6 coefficients from this estimate, which agree to within 10% with accepted values, see Tab. III. Since the total scattering cross section scales as $(C_6)^{1/3}$ [46], calculations of collisional processes are only weakly sensitive to small errors in this coefficient. We also require a bond length to generate a Lennard-Jones potential for each pair of objects. In the case of the ^{225}Ra simulation, we estimate this by adding the atomic radius of Ra (2.15 \AA) to the effective radius of the other object. While not precise, in these simulations the final results are insensitive to the exact details of the short-range interaction since such a low impact parameter collision is certain to alter the trajectory and/or eject the ^{225}Ra atom from the MOT.

	Ra	Ba	H ₂	Ar
$U(\text{eV})$	2.57	2.53	15.43	15.76
$\alpha(\text{\AA}^3)$	37.9	39.7	0.8042	1.63
Ra	2770 <i>3042 [47]</i>	2870	101	205
Ba		2980 <i>3110 [48]</i>	104	211
H ₂			7.48 <i>7.29 [49]</i>	15.3 <i>16.6 [50]</i>
Ar				31.3 <i>34.8 [51]</i>

TABLE III. Table of C_6 coefficients calculated using the London dispersion formula. All entries are in eV \AA^6 . Accepted values listed in italics and are in agreement with our estimated values to within 10%. The values for H₂ are for its vibrational ground state.